Thin films of topological nodal line semimetals as a candidate for efficient thermoelectric converters

Masashi Hosoi,[1,*] Ikuma Tateishi,[1,2] Hiroyasu Matsuura,[1] and Masao Ogata[1]
[1]*Department of Physics, University of Tokyo, 7-3-1 Hongo, Bunkyo, Tokyo 113-0033, Japan*
[2]*RIKEN Center for Emergent Matter Science, Wako, Saitama 351-0198, Japan*

(Received 19 July 2021; revised 7 October 2021; accepted 28 January 2022; published 7 February 2022)

Thermoelectric materials have attracted significant interest owing to their wide range of applications, such as power generators and refrigerators. Along with the evaluation of Bi_2Te_3 and its alloys, the search for materials that show good thermoelectric performance has risen considerably. The efficiency of thermoelectric conversion is quantified by the figure of merit, ZT, and ZT greater than unity has been considered as a target. For a large ZT, acquiring a large Seebeck coefficient and a reduction of phonon thermal conductivity are significant given its definition. In this work, we propose that a thin film of topological nodal line semimetals can be a new and promising thermoelectric material. We also discuss the correlation effect and spin current induced by the temperature gradient. The obtained results give various insights into the quest for the best thermoelectric materials.

DOI: 10.1103/PhysRevB.105.085406

I. INTRODUCTION

Exploring materials for efficient thermoelectric conversion has been a central issue in achieving sustainable energy solutions [1,2]. In particular, from a global environmental perspective, there is an urgent pursuit of materials that can efficiently generate electricity from waste heat. Driven by increasing demand, much effort has been directed toward the search for materials with a high figure of merit (ZT) [see Eq. (3)], and there have also been numerous theoretical studies discussing its physical limits [3–11]. Examples include bismuth telluride alloys, which are widely used as a thermoelectric device under 500 K and show $ZT \sim 1$ at around room temperature [12], and lead telluride alloys, for which high ZT reaching $\sim$2.2 at 915 K is reported [13–15]. However, the use of tellurium included in both materials has problems due to its toxicity and rarity. Although many candidate materials that show a large ZT have been found recently, with the exception of tellurium [16,17], the discovery of other promising materials is still highly anticipated.

One of the strategies for improving thermoelectric performance is lowering dimension. Thin films of thermoelectric materials offer a good platform to investigate in such a low-dimensional effect [18–20]. To date, two mechanisms are proposed for the enhancement of ZT in thin films. One is to use the quantum size effect, which can lead to an increase in the density of states (DOS) around Fermi energy [21,22]. When the thickness of the film is comparable to the effective de Broglie wavelength of electrons, their motion is restricted in the two-dimensional plane, yielding a remarkable change in the DOS. Theoretically, Mahan and Sofo proposed that a sharp and large DOS leads to an improvement in the Seebeck coefficient [23], and many experiments also support this prediction [24–28]. For example, in high-quality $Pb_{1-x}Eu_xTe/PbTe$ multiple quantum wells, the figure of merit $ZT > 1.2$, several times larger than the bulk value [24]. A recent study showed that $ZT > 2.4$ is expected in a high-density two-dimensional electron gas confined in a unit-cell layer thickness of $SrTiO_3$ [27]. The second mechanism is to use the phonon-blocking/electron-transmitting nature of superlattices. To maximize the figure of merit, the phonon thermal conductivity is largely suppressed because of the acoustic mismatch between superlattice components. This effect is experimentally confirmed: $ZT \sim 2.4$ at 300 K in p-type Bi_2Te_3/Sb_2Te_3 superlattices [18].

In this paper, we propose that the aforementioned two key factors to enhance ZT, i.e., the sharp DOS near the Fermi energy and reducing lattice contributions to the thermal current, are simultaneously realized in topological semimetals.

Starting from the Weyl and Dirac semimetals, the interest in topological semimetals has been extended to those with line nodes, namely, topological nodal line semimetals (TNLS) [29–37]. It is known that there are two types of explanations for TNLS—the orbital basis and the spin basis. In the orbital basis TNLS, the nodal line structure appears independent of the spin degree of freedom, and we assume the spin-orbit coupling is weak. Meanwhile, the spin basis TNLS has a strong spin-orbit coupling, and thus the spin degree of freedom is essential for the nodal line. The first material realization of TNLS is ZrSiS and $PbTaSe_2$, where ZrSiS is explained well by the orbital basis and $PbTaSe_2$ by the spin basis [34,36]. Thereafter, many materials, such as the Ca_2As and Ag_2S family, have been examined (both are the orbital basis) [38,39]. A notable property of TNLS is that they possess drumhead surface states. The nature of their dispersion is less dispersive than those of the bulk bands and their two-dimensionality yields a sharp and large DOS at the Fermi energy. Furthermore, it is expected that these surface states are robust against disorder because they are topologically protected. Thus we

*hosoi@hosi.phys.s.u-tokyo.ac.jp.

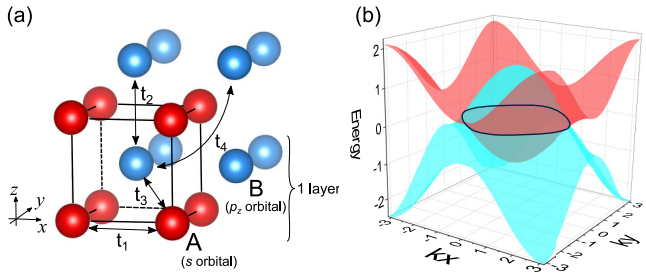

FIG. 1. (a) Schematic of the tight-binding model on the primitive tetragonal lattice for TNLS [42]. Yellow (green) spheres describe the A(B) sublattice with $s(p_z)$ orbitals and four different types of transfer integral are denoted by t_1-t_4. (b) Band dispersions of the bulk Hamiltonian at $k_z = 0$ with $E_0^A = -E_0^B = -1.5, t_1 = 0.5, t_2 = -0.5, t_3 = 0.3$, and $t_4 = -0.2$. The nodal line is depicted by a black solid line.

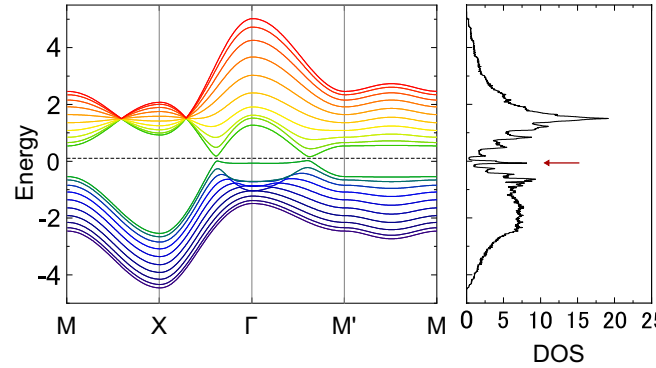

FIG. 2. Band structures of a 10-layer film of TNLS for the type I truncation along the high-symmetry points of the Brillouin zone. The coordinates (k_x, k_y) are defined as $\Gamma = (0, 0)$, $\mathrm{M} = (\pi, 0)$, $\mathrm{M}' = (0, \pi)$, and $\mathrm{X} = (\pi, \pi)$, respectively. The dashed lines describe the position of the Fermi energy. The right panel shows the DOS, and the red arrow indicates a sharp behavior supported by drumhead flat surface states.

could reduce the phonon thermal conductivity while keeping the electron contributions unchanged. We study the thermoelectric transport properties of the thin films of TNLS to find the large ZT of over 10. Moreover, we discuss the possibility of surface magnetism and a spin current [40,41].

II. MODEL

We construct a simple tight-binding model on the primitive tetragonal lattice as an example for the orbital basis TNLS. Similar results of the large Seebeck coefficient will be obtained in any TNLS. As schematically shown in Fig. 1(a), we assume that each primitive cell hosts two sublattices A and B, which possess s and p_z orbitals, respectively, and four types of transfer integrals t_1-t_4 are considered. The Hamiltonian is given by

$$H = \sum_{i,\sigma,\alpha=A,B} E_0^\alpha c_{i\sigma}^{\alpha\dagger} c_{i\sigma}^{\alpha} + \sum_{\langle i,j\rangle,\sigma} \left(t_1 c_{i\sigma}^{A\dagger} c_{j\sigma}^{A} + t_2 c_{i\sigma}^{B\dagger} c_{j\sigma}^{B} + \mathrm{H.c.}\right) + t_3 \sum_{\langle i,j\rangle,\sigma} \left(\eta_{ij} c_{i\sigma}^{A\dagger} c_{j\sigma}^{B} + \mathrm{H.c.}\right) + t_4 \sum_{\langle\langle i,j\rangle\rangle,\sigma} \left(c_{i\sigma}^{B\dagger} c_{j\sigma}^{B} + \mathrm{H.c.}\right). \tag{1}$$

Here $c_{i\sigma}^{\alpha\dagger}(c_{i\sigma}^{\alpha})$ is a creation (annihilation) operator of electrons of α sublattice with spin σ in the i-th unit cell; E_0^α is a one-body potential of each sublattice. Note that the spin degree of freedom σ represents the real spin of electrons. The sign factor $\eta_{ij} = 1(-1)$ if the site i and j belongs to the same (different) layer owing to a symmetry requirement. Note that the transfer integral t_4 is not necessary for describing TNLS. This term is introduced to make each band dispersive because, when $t_4 = 0$, one of the bands becomes exactly flat in the entire Brillouin zone. Hereafter we set $E_0^A = -E_0^B = -1.5, t_1 = 0.5, t_2 = -0.5, t_3 = 0.3$, and $t_4 = -0.2$. Throughout the remainder of this paper, the energy scales are in units of eV.

In this tight-binding model, we can find the nodal line with a spin degeneracy (e.g., Dirac nodal line) protected by the time-reversal and inversion symmetry (see Appendix A). In addition, the mirror plane existing on the x-y plane guarantees the nodal loop on the k_x-k_y plane [Fig. 1(b)]. Therefore the drumhead surface states are expected to appear on the (001) surface. To discuss its effect on thermoelectric transport, we consider thin films with two different types of truncations: In type I truncation, the top surface is terminated by a sublattice B layer and in type II by a sublattice A layer. The bottom surface is terminated by a sublattice A layer for both cases. Hereafter we focus on the type I truncation case and the explanation for type II, which does not have the surface states, is given in the Appendix B. Figure 2 shows the band structure of a 10-layer film along the high-symmetry points of the Brillouin zone and its DOS. We approximate the DOS by the following formula: $D(E) = \sum_{n,\boldsymbol{k}} \delta(E - \epsilon_{\boldsymbol{k}}^n) = \sum_{n,\boldsymbol{k}} \lim_{\Delta\to 0} \frac{\Delta/\pi}{(E-\epsilon_{\boldsymbol{k}}^n)^2+\Delta^2}$, where n is a band index and we set $\Delta = 0.01 t_1$ in the numerical calculation. We find that drumhead surface states are realized, whose flatness leads to a sharp DOS near the Fermi energy. Note that the flatness of the drumhead surface state is not guaranteed by the symmetry, and significant bending of it will reduce the DOS. However, our theories remain valid if the bending is not severe. The dispersion of the surface states is mainly determined by parameters such as the one-body potential and the transfer integrals. In the presence of the charge-neutral condition, the surface states tend to appear near the Fermi level, so the feasibility of flat surface bands is guaranteed to some extent. Additionally, we believe that the flat surface state in real materials is plausible. For instance, an analysis on a tight-binding model for a TNLS Ca_3P_2 derived from *ab initio* DFT calculations indicated the presence of a flat surface state and a sharp DOS peak associated with it [43].

III. LINEAR-RESPONSE THEORY

The linear responses of the electrical current $\boldsymbol{J}_e$ and thermal current $\boldsymbol{J}_Q$ to the electric field $\boldsymbol{E}$ and temperature gradient ∇T are given as $\boldsymbol{J}_e = L_{11}\boldsymbol{E} + L_{12}(-\nabla T/T)$ and $\boldsymbol{J}_Q = L_{21}\boldsymbol{E} + L_{22}(-\nabla T/T)$, where L_{ij} are thermoelectric transport coefficients. L_{11} is the electric conductivity σ. The Seebeck coefficient S and the thermal conductivity κ_e due to electrons

are represented as

$$S = \frac{L_{12}}{TL_{11}} = \frac{L_{12}}{T\sigma}, \quad \kappa_e = \frac{1}{T}\left(L_{22} - L_{12}L_{11}^{-1}L_{21}\right). \tag{2}$$

The efficiency of thermoelectric energy converters is evaluated by a dimensionless figure of merit:

$$ZT = \frac{S^2\sigma}{\kappa}T, \tag{3}$$

where κ is the total thermal conductivity of contributions from electrons κ_e and phonons $\kappa_{\rm ph}$. In the following, we consider only κ_e, so that our ZT is the maximum (or most optimistic) value. This assumption is justified by the following reasons. It is well known that introducing impurities or defects suppresses the phonon propagation. In TNLS, the surface states are expected to be robust against disorder unless they exist on the surface or break the time-reversal symmetry because of their topological nature. In principle, the disorder or impurity breaks the inversion symmetry, which protects the surface states. However, it does not matter as long as its effect is weak. Meanwhile, if there exists much of an amount of disorders on the surface, the surface states will be broken because the wave function of the surface states is mainly composed of surface atoms. Thus we consider a situation where the surface is clean and there exist disorders or impurities in the bulk. In this paper, we incorporate the effect of bulk disorders through relaxation time τ. We anticipate that bulk disorders will have a greater impact on the phonon transport relaxation time than on electron transport relaxation time because the contribution from surface electrons, which are unaffected by bulk disorders, is dominant in electron transport while the contribution from the bulk is dominant in phonon transport. Therefore if we introduce a certain amount of nonmagnetic impurities in the bulk and reduce the phonon propagation, we can reduce $\kappa_{\rm ph}$ while L_{12}, because the surface states are unchanged. Although the extent to which the introduction of impurities suppresses the phonon thermal conductivity depends on the materials, neglecting $\kappa_{\rm ph}$ in ZT is reasonable because of the first theoretical proposal. We will provide a brief quantitative estimation on this matter later.

In the simplest approximation or constant relaxation time approximation, the electric conductivity along the x direction is given by

$$L_{11} = \frac{4\tau e^2}{\hbar^2 V}\sum_{n,\boldsymbol{k}} \frac{\partial\epsilon_{\boldsymbol{k}}^n}{\partial k_x}\frac{\partial\epsilon_{\boldsymbol{k}}^n}{\partial k_x}\left[-f'\left(\epsilon_{\boldsymbol{k}}^n\right)\right], \tag{4}$$

where n is a band index, τ is a relaxation time, $e(<0)$ is the electron charge, and $f(\epsilon) = 1/(e^{(\epsilon-\mu)/k_BT}+1)$ is the Fermi distribution function with chemical potential μ. In the thin film case, the summation over $\boldsymbol{k}$ is in the two-dimensional space (see Appendix C for the detailed derivation). To calculate the thermoelectric transport coefficients, we use the following relations derived from the Boltzmann equation [44–47],

$$L_{12} = \frac{4\tau e}{\hbar^2 V}\sum_{n,\boldsymbol{k}} \frac{\partial\epsilon_{\boldsymbol{k}}^n}{\partial k_x}\frac{\partial\epsilon_{\boldsymbol{k}}^n}{\partial k_x}\left[-f'\left(\epsilon_{\boldsymbol{k}}^n\right)\right]\left(\epsilon_{\boldsymbol{k}}^n-\mu\right),$$

$$L_{22} = \frac{4\tau}{\hbar^2 V}\sum_{n,\boldsymbol{k}} \frac{\partial\epsilon_{\boldsymbol{k}}^n}{\partial k_x}\frac{\partial\epsilon_{\boldsymbol{k}}^n}{\partial k_x}\left[-f'\left(\epsilon_{\boldsymbol{k}}^n\right)\right]\left(\epsilon_{\boldsymbol{k}}^n-\mu\right)^2. \tag{5}$$

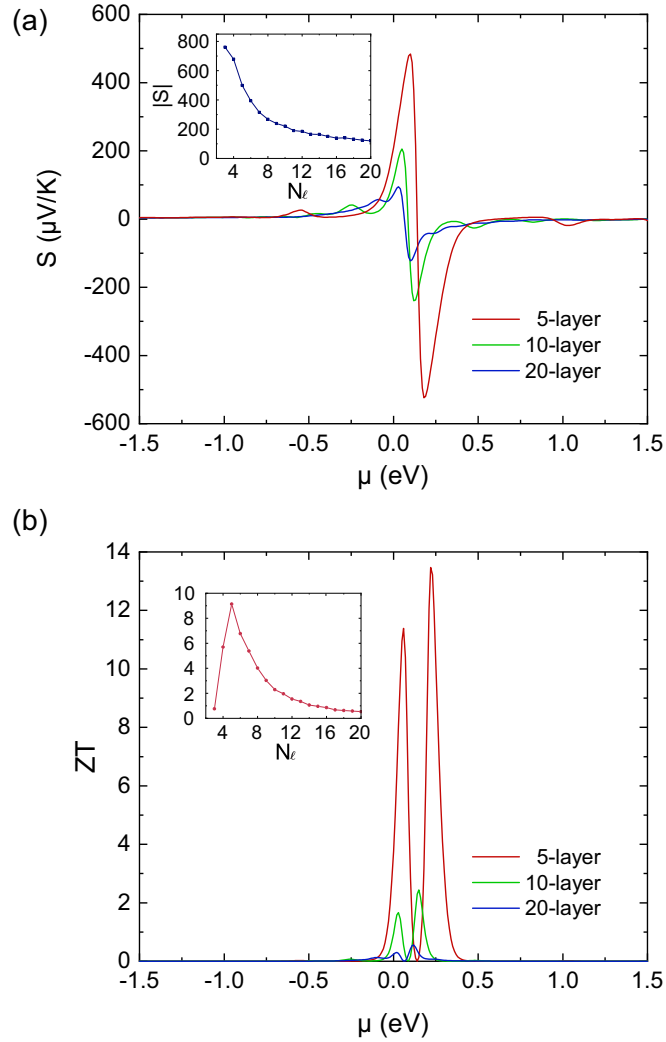

FIG. 3. Chemical potential dependence of the thermal coefficients in the thin films of TNLS at around room temperature ($k_BT = 2.5\times10^{-2}$). (a) Seebeck coefficient. (b) Figure of merit. Red, green, and blue solid lines describe the result for 5-layer, 10-layer, and 20-layer films with the type I truncation, respectively. (Inset) Layer-number (N_ℓ) dependence of S and ZT, where the chemical potential is set at the Fermi energy.

The derivations are microscopically justified when we do not take into account the phonon heat current originating from the phonon drag and heat currents due to a long-range Coulomb interaction or electron–phonon interactions [48–50] and when the relaxation rate $\Gamma = \hbar/2\tau$ is very small compared with $\epsilon_{\boldsymbol{k}}^n$.

IV. THERMOELECTRIC TRANSPORT PROPERTIES OF TNLS

Figure 3(a) shows the chemical potential dependence of the Seebeck coefficient with various thickness at around room temperature, $k_BT = 2.5\times10^{-2}$. The red, green, and blue solid lines represent the result for 5-layer, 10-layer, and 20-layer films with the type I truncation, respectively. A large Seebeck coefficient is observed near the Fermi energy and it becomes larger as the film gets thinner (see the inset, where N_ℓ is the number of layers). We note that the wave function is well

localized at the top and bottom layers and the penetration into the bulk is negligible; thus the "surface state" is well defined even for the 5-layer film.

Figure 3(b) shows the corresponding ZT with $\kappa_{\rm ph}$ being neglected. We find giant ZT with more than 13 for the type I 5-layer film, which is five times larger than Bi_2Te_3/Sb_2Te_3 superlattices. Note that the peak position is almost identical to the Fermi energy of the half-filled system.

When $\mu = 0$, the sharp DOS peak due to the drumhead surface states is below the chemical potential so that the sign of S is positive (holelike). As μ increases, S changes its sign to negative (electronlike), which is probably due to the DOS peak above the chemical potential. As shown in Appendix B, in the type II truncation case where there is no drumhead surface states, a similar behavior of S as a function of μ is observed, but with small absolute values. This means that the existence of the drumhead surface states strongly enhances the absolute value of S and ZT.

The dependence on the number of layers N_ℓ is shown in the inset, where the chemical potential is set at the Fermi energy. The Seebeck coefficient S [inset of Fig. 3(a)] monotonically decreases, while ZT [inset of Fig. 3(b)] hits the maximum at $N_\ell = 5$ and then decreases as the film thickens. The behavior for $N_\ell \geqslant 5$ is approximated as $S \sim N_\ell^{-1}$ and $ZT \sim N_\ell^{-2}$, respectively. These results are roughly explained by the band structures for each layer size. In thin films, the DOS peak at around the Fermi energy is conspicuous compared with the DOS peak in thick films because the DOS originating from the bulk bands is not so large. This sharp DOS peak contributes to the large Seebeck effect and to the giant figure of merit. However, when the film is too thin, i.e., $N_\ell < 5$, the finite-size gap becomes large and the surface states are not distinguishable from the bulk bands, which leads to an almost zero conductivity and a disappearance of the DOS peak. Therefore ZT becomes small.

Here we provide a rough comparison to the real materials. In ZrSiS hosting of a Dirac nodal line around the Γ point in the Brillouin zone similar to our model, it is reported that the phonon contribution to the thermal conductivity is almost ten times larger than the electron contribution [51]. Thus the obtained ZT would be a tenth of our results, i.e., at most $ZT \sim 1$. However, we will be able to improve this value to some extent in the dirty limit. It should be noted that the extent to which the impurities reduce the thermal conductivity is unknown, and experimental confirmation is required.

V. SURFACE MAGNETISM AND SPIN CURRENT

Next we discuss the effect of electron correlation. Because of the large DOS at the surface of the type I film, the Coulomb interaction is strongly screened and an on-site Hubbard type interaction, $H_U = \sum_{i,\alpha=A,B} U_\alpha n^\alpha_{i\uparrow} n^\alpha_{i\downarrow}$ well describes the effects of correlation. Here $n^\alpha_{i\sigma} = c^{\alpha\dagger}_{i\sigma} c^\alpha_{i\sigma}$ is a number operator. In this paper, we evaluate the effects of the Hubbard interaction in an unrestricted Hartree–Fock approximation. Quantum fluctuation, which is not taken into account here, is expected to just reduce magnetic moments and not to change the results qualitatively.

Starting from initial spin configurations with Néel and ferromagnetic order, we solve the self-consistent equations for the mean-field parameters $\langle n^\alpha_{\ell\sigma}\rangle$, with ℓ being a layer index. We determine the ground state by comparing the mean-field energy $\langle H_{\rm mf}\rangle$. Then we calculate the magnetization for each layer to discuss the surface magnetism. For simplicity, we set $U_A = U_B = U$. As shown in Fig. 4(a), we find five phases as a function of U, including surface ferromagnetic (SF) orders. Particularly in the SF-I phase, only the top surface at which the drumhead surface states localize acquires the magnetic polarization. The detailed magnetic structures for other phases are given in Appendix E. Note that the ground state is obtained from the initial state with Néel order for a full range of U. The phase boundaries are determined by singular points of the second differentiation of the mean-field energy $\partial^2\langle H_{\rm mf}\rangle/\partial U^2$. We comment that a similar SF phase is found in the previous study for the different TNLS model [40].

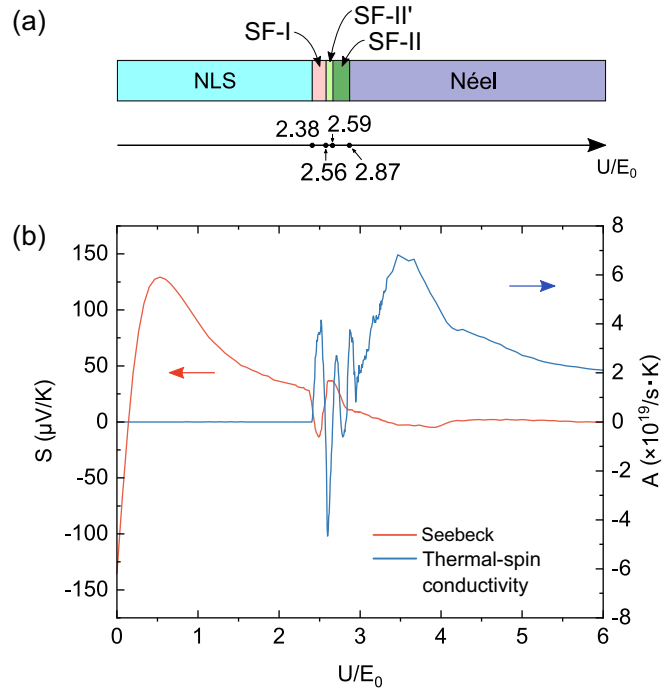

FIG. 4. Effects of correlation on the film of TNLS. (a) Phase diagram of 10-layer film of TNLS with type I truncation in the U parameter space. SF denotes the SF order and NLS denotes the nodal line semimetal phase. The magnetic structures for each phase are shown in Appendix E. The horizontal axis is normalized by the one-body potential E_0. (b) Seebeck and thermal-spin conductivity. Orange (blue) solid line corresponds to the left (right) axis and describes the results for the Seebeck coefficient (thermal-spin conductivity).

Considering that magnetically polarized electrons support the spin current, we expect that the thermal-spin conductivity defined below is also enhanced in the SF phases. Note that the relation Eq. (5) holds even in the presence of the Hubbard interaction [49]. The spin current $\boldsymbol{J}_s$ is defined as

$$\boldsymbol{J}_s = \frac{1}{e}(\boldsymbol{J}_e^\uparrow - \boldsymbol{J}_e^\downarrow) = \sum_{\boldsymbol{k},\sigma} \sigma \left(\frac{\partial \epsilon_{\boldsymbol{k}\sigma}}{\partial \hbar \boldsymbol{k}}\right) c^\dagger_{\boldsymbol{k}\sigma} c_{\boldsymbol{k}\sigma}. \tag{6}$$

As in the case of the ordinary Seebeck effect, applying a condition that the electrical current is zero, we obtain

$$\boldsymbol{J}_s = \frac{1}{e}\frac{2(L_{11}^{\uparrow}L_{12}^{\downarrow} - L_{11}^{\downarrow}L_{12}^{\uparrow})}{L_{11}^{\uparrow} + L_{11}^{\downarrow}}\frac{\nabla T}{T} \equiv A\nabla T, \tag{7}$$

where we call A the thermal-spin conductivity [41].

The ordinary Seebeck coefficient and A are shown in Fig. 4(b). Note that the chemical potential is determined by the half-filled condition for each U, and the absolute value of A is proportional to τ, which is assumed to be 10^{-13} s in Fig. 4. There is a drastic sign change of S at small U. This is because the one-body potential energy becomes layer dependent owing to Coulomb interaction, and thus the energy shift of the state occurs. As the system enters into an SF phase, we find a finite thermal-spin conductivity and it shows an oscillation while the system is in the SF phases. The positions where the sign changes occur correspond to the phase transition points. Although the ordinary Seebeck coefficient shows a similar characteristic behavior, the thermal-spin conductivity is more sensitive to the change in magnetization. However, contrary to our expectations, the thermal-spin conductivity hits its maximum in the Néel phase and not in the SF phase. This is because the difference in the magnetizations in the A and B sublattices remains quite large in the region $3.0 \lesssim U/E_0 \lesssim 4.0$. Note that if the ferromagnetic phase were stable at large U, the thermal-spin conductivity would be finite only for the SF phases, as is the case for a one-dimensional quantum wire [41]. Constructing such a situation and material realization will be a future perspective.

VI. DISCUSSION AND SUMMARY

To summarize, we have shown that thin films of TNLS are a promising candidate for thermoelectric converters. Unlike the usual semiconductors, a peculiar DOS structure due to the drumhead surface states results in nonvanishing and large Seebeck coefficient at the Fermi energy. Because the surface states are robust against disorders in the bulk, we can reduce the phonon contribution to the thermal conductivity, which leads to a giant ZT. In our setup, we have found ZT with more than 13 for the type I 5-layer film. A remarkable point is that we can easily tune the chemical potential by applying the gate voltage in the film, and thus we can find the maximum of ZT experimentally. We have also analyzed the correlation effect and figured out a nonzero thermal-spin conductivity for finite U. However, the way to enhance the same is a concern that still needs to be addressed.

In real materials, Ag_2S will be a good candidate for the realization of the present theoretical prediction, where the existence of almost flat drumhead surface states is reported [39]. Thus we expect that a similar situation would be realized in this material and a giant ZT would be obtained for thin films.

ACKNOWLEDGMENTS

This work is supported by Grants-in-Aid for Scientific Research from JST-Mirai Program Grant No. JPMJMI19A1, Japan, and the Japan Society for the Promotion of Science (No. JP20J10725, No. JP20K03802, No. JP18H01162, and No. JP18K03482). M.H. was supported by the Japan Society for the Promotion of Science through the Research Fellowships for Young Scientists and the Program for Leading Graduate Schools (MERIT).

APPENDIX A: SYMMETRY OPERATORS

The momentum space Hamiltonian corresponding to Eq. (1) is given by

$$H_{\boldsymbol{k}} = \begin{pmatrix} E_0^A + 2t_1(\cos k_x + \cos k_y + \cos k_z) & 8it_3 \cos\frac{k_x}{2}\cos\frac{k_y}{2}\sin\frac{k_z}{2} \\ -8it_3 \cos\frac{k_x}{2}\cos\frac{k_y}{2}\sin\frac{k_z}{2} & E_0^B + 2t_2\cos k_z + 4t_4\cos k_z(\cos k_x + \cos k_y) \end{pmatrix}. \tag{A1}$$

The inversion operator I and the mirror operator m_z are represented by the z component of the Pauli matrix σ_z.

APPENDIX B: BAND STRUCTURES OF THE TYPE II FILM AND THERMAL TRANSPORT PROPERTIES

This section describes the band structures for the type II truncation case in TNLS films and examines their thermal transport properties. The band structure for the type II case is shown in Fig. 5(a). The projected bulk nodal line is a gapless point, as in the type I case. However, in contrast with the type I case, midgap surface states were not found. We can explain this difference from the perspective of the topological materials.

In our model, the band inversion at the Γ point occurs between two bands with different parities so the $\mathbb{Z}_2$ index [52,53] is calculated as $(1;111)$. This index represents a TNLS in a case where spin-orbit coupling is negligible and a strong topological insulator in a case where spin-orbit coupling is significant.. In TNLSs, the $\mathbb{Z}_2$ index is directly related to the Zak phase. In this case, the Zak phases at the surface Γ point and the surface X points differ by π. This difference in the Zak phase corresponds to the difference in the number of occupied bands at the Γ and X points. A band localized at the surface [54] actually crosses the Fermi energy near the gapless points. However, the Zak phase does not guarantee that the band will be a "midgap" surface state. The detailed energy of the band depends on the surface parameters. In our thin film model, we use the same parameters as the bulk model, so the band is located at the upper edge of the bulk occupied band spectrum in the type II case.

However, in realistic materials, the surface parameters may change when the surface is made. Therefore the surface state tends to appear as an isolated midgap state. For example, in our model, the type II film does not have the same number of A and B sites. In realistic materials, this corresponds to an imbalance between donors and acceptors. This can change the one-body potential of the A site on the surface, and the band

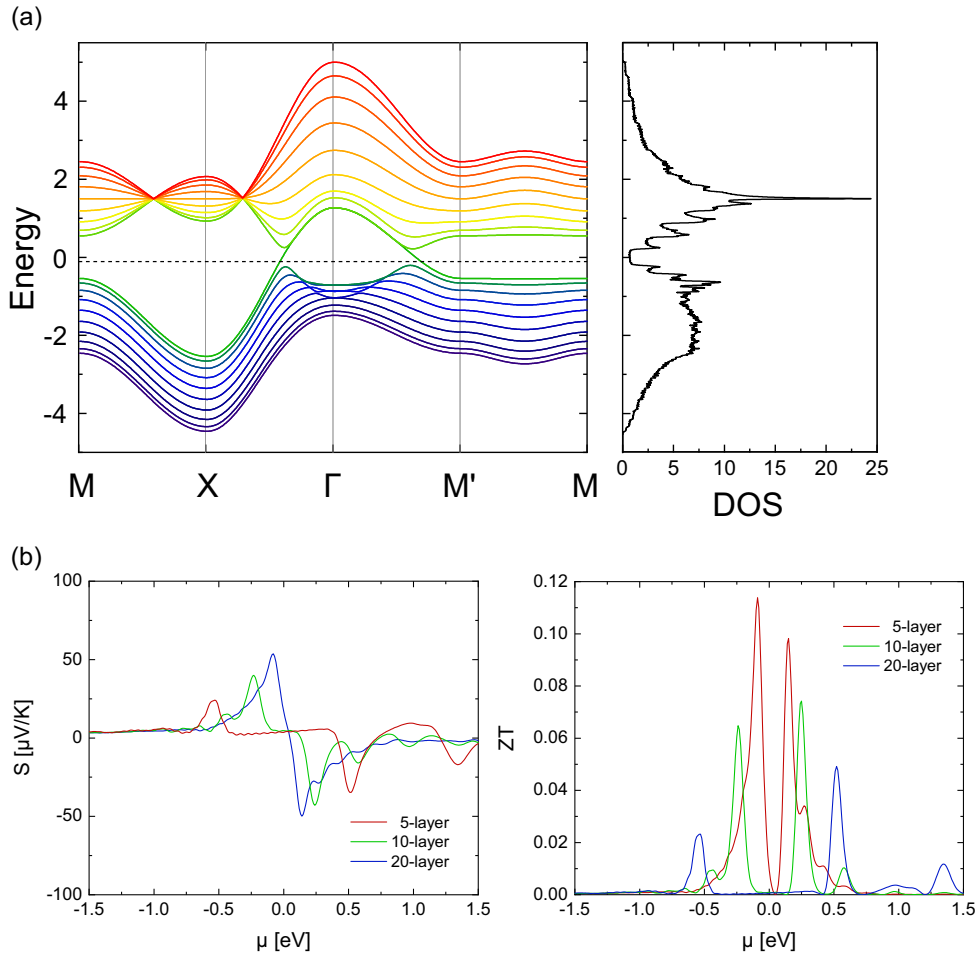

FIG. 5. (a) Band structures of a 10-layer TNLS film with type II truncation along the high-symmetry points of the Brillouin zone. The coordinates of the high-symmetry points are given in the caption of Fig. 2. The dashed line represents the Fermi energy. The right panel shows the DOS. (b) Chemical potential dependence of the Seebeck coefficients S and ZT for the type II TNLS film. Red, green, and blue lines represent the results for 5-, 10-, and 20-layer films, respectively.

localized on the surface at the X point (and M point) can shift toward the Fermi energy. This is why drumhead surface states in TNLSs have been experimentally observed and reported in many previous studies, as explained in the main text.

The thermoelectric transport properties and figure of merit (ZT) for type II films with various thicknesses are shown in Figs. 5(b) and 5(c). The temperature is set to approximately room temperature, $k_BT = 2.5 \times 10^{-2}$. In contrast with the type I case, the absolute value of S and the layer dependence are small, which results in a banal value of ZT. However, in realistic materials, we can expect large values of S and ZT, even for the type II case, because of the surface reconstruction described above.

APPENDIX C: DETAILED DERIVATION OF L_{11}

In this section, we present a detailed derivation of L_{11}. The electric conductivity L_{11} under a uniform electric field is obtained from the equation

$$L_{11} = \left.\frac{\Phi_{\mu\nu}(\omega) - \Phi_{\mu\nu}(0)}{i(\omega + i\delta)}\right|_{\omega\to 0}, \tag{C1}$$

where $\Phi_{\mu\nu}(\omega) = \Phi_{\mu\nu}(i\omega_\lambda)|_{i\omega_\lambda\to\hbar\omega+i\delta}$. The quantities ω and ω_n are the frequency and Matsubara frequency, respectively, and $i\omega_\lambda \to \hbar\omega + i\delta$ describes the analytic continuation. If the vertex correction is negligible, then

$$\begin{aligned}\Phi_{\mu\nu}(i\omega_\lambda) &= \frac{1}{V}\int_0^\beta d\tau \langle T_\tau \hat{j}_\mu(\tau)\hat{j}_\nu(0)\rangle e^{i\omega_\lambda\tau} \\ &= -\frac{2e^2k_BT}{\hbar^2V}\sum_{n,\boldsymbol{k}} \frac{\partial\epsilon_{\boldsymbol{k}}}{\partial k_\mu}\mathcal{G}(\boldsymbol{k}, i\epsilon_n - i\omega_\lambda)\frac{\partial\epsilon_{\boldsymbol{k}}}{\partial k_\nu}\mathcal{G}(\boldsymbol{k}, i\epsilon_n),\end{aligned} \tag{C2}$$

where the thermal Green's function within a constant relaxation time approximation is

$$\mathcal{G}(\boldsymbol{k}, i\epsilon_n) = \frac{1}{i\epsilon_n - \epsilon_{\boldsymbol{k}} + \mu + \frac{i\hbar}{2\tau}\mathrm{sgn}(\epsilon_n)}. \tag{C3}$$

Taking the Matsubara summation using a residue integral and analytical continuation $i\omega_\lambda \to \hbar\omega + i\delta$, we

obtain

$$\Phi_{\mu\nu}(\omega) = \frac{2e^2}{\hbar^2 V}\sum_{\boldsymbol{k}}\frac{\partial\epsilon_{\boldsymbol{k}}}{\partial k_\mu}\frac{\partial\epsilon_{\boldsymbol{k}}}{\partial k_\nu}\int_{-\infty}^{\infty}\frac{d\epsilon}{2\pi i}f(\epsilon) \times [G^R(\boldsymbol{k},\epsilon)G^R(\boldsymbol{k},\epsilon_+) - G^A(\boldsymbol{k},\epsilon)G^R(\boldsymbol{k},\epsilon_+) + G^A(\boldsymbol{k},\epsilon_-)G^R(\boldsymbol{k},\epsilon) - G^A(\boldsymbol{k},\epsilon_-)G^A(\boldsymbol{k},\epsilon)]. \tag{C4}$$

Here, $G^A(\boldsymbol{k},\epsilon) = G^{R*}(\boldsymbol{k},\epsilon)$ and $\epsilon_\pm = \epsilon \pm \hbar\omega$. Therefore

$$L_{11} = \frac{1}{i\omega}\frac{2e^2}{\hbar^2 V}\sum_{\boldsymbol{k}}\frac{\partial\epsilon_{\boldsymbol{k}}}{\partial k_\mu}\frac{\partial\epsilon_{\boldsymbol{k}}}{\partial k_\nu}\int_{-\infty}^{\infty}\frac{d\epsilon}{2\pi i}f(\epsilon)(\hbar\omega) \times\left[(G^R - G^A)\frac{\partial}{\partial\epsilon}(G^R - G^A)\right] = \frac{2e^2}{\pi\hbar V}\sum_{\boldsymbol{k}}\frac{\partial\epsilon_{\boldsymbol{k}}}{\partial k_\mu}\frac{\partial\epsilon_{\boldsymbol{k}}}{\partial k_\nu}\int_{-\infty}^{\infty}d\epsilon\left(-\frac{\partial f}{\partial\epsilon}\right)[\mathrm{Im}G^R(\boldsymbol{k},\epsilon)]^2. \tag{C5}$$

Inserting $G^R(\boldsymbol{k},\epsilon) = 1/(\epsilon - \epsilon_{\boldsymbol{k}} + i\hbar/2\tau)$ and executing a residue integral finally gives

$$L_{11} = \frac{4\tau e^2}{\hbar^2 V}\sum_{\boldsymbol{k}}\frac{\partial\epsilon_{\boldsymbol{k}}}{\partial k_\mu}\frac{\partial\epsilon_{\boldsymbol{k}}}{\partial k_\nu}(-f'(\epsilon_{\boldsymbol{k}})). \tag{C6}$$

APPENDIX D: MEAN-FIELD APPROXIMATION

In the mean-field approximation, the Hubbard interaction is decoupled into

$$H_U \sim \sum_{i,\alpha=A,B} U_\alpha\left(\langle n^\alpha_{i\uparrow}\rangle n^\alpha_{i\downarrow} + n^\alpha_{i\uparrow}\langle n^\alpha_{i\downarrow}\rangle - \langle n^\alpha_{i\uparrow}\rangle\langle n^\alpha_{i\downarrow}\rangle\right). \tag{D1}$$

When we ignore particle number deviations within the same layer, the mean-field parameters are the layer, sublattice, and spin indices. Then, the values of the $4N_\ell$ parameters are determined by a self-consistent calculation, where N_ℓ is the number of layers, and we set $N_\ell = 10$.

Once the self-consistent equations are solved, we can define the magnetization for each layer and sublattice as

$$M^\alpha_\ell = \langle n^\alpha_{\ell\uparrow}\rangle - \langle n^\alpha_{\ell\downarrow}\rangle, \tag{D2}$$

where ℓ is the index of the layer. Moreover, the full Hamiltonian can be divided into

$$H = H_\uparrow \oplus H_\downarrow. \tag{D3}$$

Then, the thermoelectric transport coefficients L^σ_{ij} are calculated using the energy spectrum of H_σ.

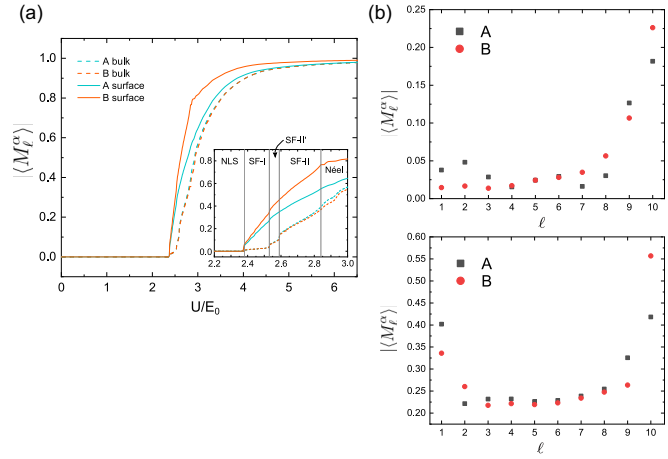

FIG. 6. (a) Correlation U dependence of the surface and bulk magnetization. The blue solid (dashed) line describes the result for the sublattice A layer at the surface (bulk), and the orange lines describe the corresponding results for the sublattice B layer. Here we adopt $\ell = 10$ as the surface layer and $\ell = 5$ as the bulk layer. The inset shows an extended view around the phase transition points, and the phase boundaries are also presented. (b) Magnetization of each layer. Top: SF-I phase ($U/E_0 = 2.47$). Bottom: SF-II phase ($U/E_0 = 2.67$). The black squares (red circles) show the magnetization of sublattice A (B).

APPENDIX E: MAGNETIC STRUCTURES FOR THE FIVE PHASES IN A TNLS FILM WITH CORRELATIONS

Figure 6(a) shows the correlation dependence of the surface and bulk magnetization. When U is small, the system remains in the nodal line semimetal state, and does not exhibit finite magnetization. Subsequently, it enters into a SF phase, which we call the SF-I phase at $U/E_0 = 2.38$. In this phase, the magnetization of one side of the surface increases, and that of the other layers remains small [see the top panel of Fig. 6(b)]. It should be noted that the wave function of the drumhead surface states localize at the B sublattice of the $\ell = 10$ layer, which indicates that only the drumhead surface states are magnetically polarized. Then, we encounter two phase transitions at $U/E_0 = 2.56, 2.59$. Although the differences in the features of these two phases, which we name SF-II' and SF-II, respectively, are unclear, we find that the magnetization of both sides of the surface is more conspicuous than that of the bulk in the SF-II phase [see the bottom panel of Fig. 6(b)]. As U increases, not only the surface magnetization but also the bulk magnetization grows, and the system enters into the Néel ordered phase at $U/E_0 = 2.87$. We note that even in this Néel ordered phase, the amplitude of magnetization for each layer is not uniform and a similar property of deviation to the SF phases remains, but the difference between the surface magnetization and the bulk magnetization is reduced.

[1] G. Chen, M. S. Dresselhaus, G. Dresselhaus, J.-P. Fleurial, and T. Caillat, Recent developments in thermoelectric materials, Int. Mater. Rev. **48**, 45 (2003).

[2] J. He and T. M. Tritt, Advances in thermoelectric materials research: Looking back and moving forward, Science **357**, 6358 (2017).

[3] G. A. Slack and V. G. Tsoukala, Some properties of semiconducting $IrSb_3$, J. Appl. Phys. **76**, 1665 (1994).

[4] B. C. Sales, D. Mandrus, and R. K. Williams, Filled Skutterudite antimonides: A new class of thermoelectric materials, Science **272**, 1325 (1996).

[5] D. Mandrus, B. C. Sales, V. Keppens, B. C. Chakoumakos, P. Dai, L. A. Boatner, R. K. Williams, J. R. Thompson, T. W. Darling, A. Migliori *et al.*, Filled skutterudite antimonides: Validation of the electron-crystal phonon-glass approach to new thermoelectric materials, MRS Proc. **478**, 199 (1997).

[6] D.-Y. Chung, T. Hogan, P. Brazis, M. Rocci-Lane, C. Kannewurf, M. Bastea, C. Uher, and M. G. Kanatzidis, $CsBi_4Te_6$: A high-performance thermoelectric material for low-temperature applications, Science **287**, 1024 (2000).

[7] K. F. Hsu, S. Loo, F. Guo, W. Chen, J. S. Dyck, C. Uher, T. Hogan, E. K. Polychroniadis, and M. G. Kanatzidis, Cubic $AgPb_mSbTe_{2+m}$: Bulk thermoelectric materials with high figure of merit, Science **303**, 818 (2004).

[8] G. Tan, F. Shi, S. Hao, L.-D. Zhao, H. Chi, X. Zhang, C. Uher, C. Wolverton, V. P. Dravid, and M. G. Kanatzidis, Non-equilibrium processing leads to record high thermoelectric figure of merit in PbTe/SrTe, Nat. Commun. **7**, 12167 (2016).

[9] L. D. Hicks and M. S. Dresselhaus, Effect of quantum-well structures on the thermoelectric figure of merit, Phys. Rev. B **47**, 12727 (1993).

[10] L. D. Hicks and M. S. Dresselhaus, Thermoelectric figure of merit of a one-dimensional conductor, Phys. Rev. B **47**, 16631 (1993).

[11] D. Bayerl and E. Kioupakis, Theoretical limits of thermoelectric figure of merit in *n*-type TiO_2 polymorphs, Phys. Rev. B **91**, 165104 (2015).

[12] H. J. Goldsmid, Bismuth telluride and Its alloys as materials for thermoelectric generation, Materials **7**, 2577 (2014).

[13] Y. Pei, A. LaLonde, S. Iwanaga, and G. Jeffrey Snyder, High thermoelectric figure of merit in heavy hole dominated PbTe, Energy Environ. Sci. **4**, 2085 (2011).

[14] Y. Pei, X. Shi, A. LaLonde, H. Wang, L. Chen, and G. J. Snyder, Convergence of electronic bands for high performance bulk thermoelectrics, Nature (London) **473**, 66 (2011).

[15] K. Biswas, J. He, I. D. Blum, C.-I. Wu, T. P. Hogan, D. N. Seidman, V. P. Dravid, and M. G. Kanatzidis, High-performance bulk thermoelectrics with all-scale hierarchical architectures, Nature (London) **489**, 414 (2012).

[16] B. Hinterleitner, I. Knapp, M. Poneder, Y. Shi, H. Müller, G. Eguchi, C. Eisenmenger-Sittner, M. Stöger-Pollach, Y. Kakefuda, N. Kawamoto, Q. Guo, T. Baba, T. Mori, S. Ullah, X.-Q. Chen, and E. Bauer, Thermoelectric performance of a metastable thin-film Heusler alloy, Nature (London) **576**, 85 (2019).

[17] D. Byeon, R. Sobota, K. Delime-Codrin, S. Choi, K. Hirata, M. Adachi, M. Kiyama, T. Matsuura, Y. Yamamoto, M. Matsunami, and T. Takeuchi, Discovery of colossal Seebeck effect in metallic Cu_2Se, Nat. Commun. **10**, 72 (2019).

[18] R. Venkatasubramanian, E. Siivola, T. Colpitts, and B. O'Quinn, Thin-film thermoelectric devices with high room-temperature figures of merit, Nature (London) **413**, 597 (2001).

[19] T. C. Harman, P. J. Taylor, M. P. Walsh, and B. E. LaForge, Quantum dot superlattice thermoelectric materials and devices, Science **297**, 2229 (2002).

[20] T. C. Harman, M. P. Walsh, B. E. laforge, and G. W. Turner, Nanostructured thermoelectric materials, J. Electron. Mater. **34**, L19 (2005).

[21] M. S. Dresselhaus, G. Chen, M. Y. Tang, R. G. Yang, H. Lee, D. Z. Wang, Z. F. Ren, J.-P. Fleurial, and P. Gogna, New directions for low-dimensional thermoelectric materials, Adv. Mater. **19**, 1043 (2007).

[22] J. Mao, Z. Liu, and Z. Ren, Size effect in thermoelectric materials, npj Quantum Mater. **1**, 1 (2016).

[23] G. D. Mahan and J. O. Sofo, The best thermoelectric, Proc. Natl. Acad. Sci. USA **93**, 7436 (1996).

[24] T. C. Harman, D. L. Spears, and M. J. Manfra, High thermoelectric figures of merit in PbTe quantum wells, JEM **25**, 1121 (1996).

[25] L. D. Hicks, T. C. Harman, X. Sun, and M. S. Dresselhaus, Experimental study of the effect of quantum-well structures on the thermoelectric figure of merit, Phys. Rev. B **53**, R10493 (1996).

[26] T. C. Harman, D. L. Spears, and M. P. Walsh, PbTe/Te superlattice structures with enhanced thermoelectric figures of merit, J. Electron. Mater. **28**, L1 (1999).

[27] H. Ohta, S. Kim, Y. Mune, T. Mizoguchi, K. Nomura, S. Ohta, T. Nomura, Y. Nakanishi, Y. Ikuhara, M. Hirano, H. Hosono, and K. Koumoto, Giant thermoelectric Seebeck coefficient of a two-dimensional electron gas in $SrTiO_3$, Nat. Mater. **6**, 129 (2007).

[28] R. Y. Wang, J. P. Feser, J.-S. Lee, D. V. Talapin, R. Segalman, and A. Majumdar, Enhanced thermopower in PbSe nanocrystal quantum dot superlattices, Nano Lett. **8**, 2283 (2008).

[29] A. A. Burkov, M. D. Hook, and L. Balents, Topological nodal semimetals, Phys. Rev. B **84**, 235126 (2011).

[30] M. Phillips and V. Aji, Tunable line node semimetals, Phys. Rev. B **90**, 115111 (2014).

[31] C. Fang, Y. Chen, H.-Y. Kee, and L. Fu, Topological nodal line semimetals with and without spin-orbital coupling, Phys. Rev. B **92**, 081201(R) (2015).

[32] H. Weng, Y. Liang, Q. Xu, R. Yu, Z. Fang, X. Dai, and Y. Kawazoe, Topological node-line semimetal in three-dimensional graphene networks, Phys. Rev. B **92**, 045108 (2015).

[33] R. Yu, H. Weng, Z. Fang, X. Dai, and X. Hu, Topological Node-Line Semimetal and Dirac Semimetal State in Antiperovskite Cu_3PdN, Phys. Rev. Lett. **115**, 036807 (2015).

[34] M. Neupane, I. Belopolski, M. M. Hosen, D. S. Sanchez, R. Sankar, M. Szlawska, S.-Y. Xu, K. Dimitri, N. Dhakal, P. Maldonado, P. M. Oppeneer, D. Kaczorowski, F. Chou, M. Z. Hasan, and T. Durakiewicz, Observation of topological nodal fermion semimetal phase in ZrSiS, Phys. Rev. B **93**, 201104(R) (2016).

[35] J. Hu, Z. Tang, J. Liu, X. Liu, Y. Zhu, D. Graf, K. Myhro, S. Tran, C. N. Lau, J. Wei, and Z. Mao, Evidence of Topological Nodal-Line Fermions in ZrSiSe and ZrSiTe, Phys. Rev. Lett. **117**, 016602 (2016).

[36] G. Bian, T.-R. Chang, R. Sankar, S.-Y. Xu, H. Zheng, T. Neupert, C.-K. Chiu, S.-M. Huang, G. Chang, I. Belopolski, D. S. Sanchez, M. Neupane, N. Alidoust, C. Liu, B. Wang, C.-C. Lee, H.-T. Jeng, C. Zhang, Z. Yuan, S. Jia *et al.*, Topological nodal-line fermions in spin-orbit metal $PbTaSe_2$, Nat. Commun. **7**, 10556 (2016).

[37] M. Hirayama, R. Okugawa, T. Miyake, and S. Murakami, Topological Dirac nodal lines and surface charges in fcc alkaline earth metals, Nat. Commun. **8**, 14022 (2017).

[38] I. Tateishi, Nodal lines and mapping to mirror Chern numbers in Ca_2As family, Phys. Rev. B **102**, 155111 (2020).

[39] H. Huang, K.-H. Jin, and F. Liu, Topological nodal-line semimetal in nonsymmorphic *Cmce*-phase Ag_2S, Phys. Rev. B **96**, 115106 (2017).

[40] J. Liu and L. Balents, Correlation effects and quantum oscillations in topological nodal-loop semimetals, Phys. Rev. B **95**, 075426 (2017).

[41] M. Ogata and H. Fukuyama, Theory of spin seebeck effects in a quantum wire, J. Phys. Soc. Jpn. **86**, 094703 (2017).

[42] K. Momma and F. Izumi, Vesta 3 for three-dimensional visualization of crystal, volumetric and morphology data, J. Appl. Crystallogr. **44**, 1272 (2011).

[43] Y.-H. Chan, C.-K. Chiu, M. Y. Chou, and A. P. Schnyder, $Ca_3 P_2$ and other topological semimetals with line nodes and drumhead surface states, Phys. Rev. B **93**, 205132 (2016).

[44] G. D. Mahan, *Many-Particle Physics* (Plenum Press, New York, 1990).

[45] A. Sommerfeld and H. Bethe, *Elektronentheorie der Metalle*, Handbuch der Physik (Springer, Berlin, Heidelberg, 1933), Vol. 24/2.

[46] N. F. Mott and H. Jones, *The Theory of the Properties of Metals and Alloys* (Oxford University Press, Oxford, UK, 1936).

[47] A. H. Wilson, *The Theory of Metals* (Cambridge University Press, Cambridge, UK, 1936).

[48] M. Jonson and G. D. Mahan, Electron-phonon contribution to the thermopower of metals, Phys. Rev. B **42**, 9350 (1990).

[49] H. Kontani, General formula for the thermoelectric transport phenomena based on Fermi liquid theory: Thermoelectric power, Nernst coefficient, and thermal conductivity, Phys. Rev. B **67**, 014408 (2003).

[50] M. Ogata and H. Fukuyama, Range of validity of sommerfeld–bethe relation associated with seebeck coefficient and phonon drag contribution, J. Phys. Soc. Jpn. **88**, 074703 (2019).

[51] G. Hussain, X. Rao, N. Li, W. Chu, X. Liu, X. Zhao, and X. Sun, Electron transport in Dirac nodal-line semimetal ZrSiS, Phys. Lett. A **384**, 126938 (2020).

[52] L. Fu and C. L. Kane, Topological insulators with inversion symmetry, Phys. Rev. B **76**, 045302 (2007).

[53] Y. Kim, B. J. Wieder, C. L. Kane, and A. M. Rappe, Dirac Line Nodes in Inversion-Symmetric Crystals, Phys. Rev. Lett. **115**, 036806 (2015).

[54] D. Vanderbilt and R. D. King-Smith, Electric polarization as a bulk quantity and its relation to surface charge, Phys. Rev. B **48**, 4442 (1993).